CLIMATOLOGY

South Asian summer monsoon projections constrained by the interdecadal Pacific oscillation

Xin Huang[1,2], Tianjun Zhou[1,2,3]*, Aiguo Dai[4], Hongmei Li[5], Chao Li[5], Xiaolong Chen[1], Jingwen Lu[1,2], Jin-Song Von storch[5], Bo Wu[1,3]

A reliable projection of future South Asian summer monsoon (SASM) benefits a large population in Asia. Using a 100-member ensemble of simulations by the Max Planck Institute Earth System Model (MPI-ESM) and a 50-member ensemble of simulations by the Canadian Earth System Model (CanESM2), we find that internal variability can overshadow the forced SASM rainfall trend, leading to large projection uncertainties for the next 15 to 30 years. We further identify that the Interdecadal Pacific Oscillation (IPO) is, in part, responsible for the uncertainties. Removing the IPO-related rainfall variations reduces the uncertainties in the near-term projection of the SASM rainfall by 13 to 15% and 26 to 30% in the MPI-ESM and CanESM2 ensembles, respectively. Our results demonstrate that the uncertainties in near-term projections of the SASM rainfall can be reduced by improving prediction of near-future IPO and other internal modes of climate variability.

INTRODUCTION

The South Asian summer monsoon (SASM), the strongest component of the global monsoon system, contributes about 80% of the annual rainfall in South Asia (*1*). It provides the principal water supply for more than a billion people (*2*). Hence, being able to predict SASM variations on different time scales is vital for agriculture, ecosystems, and the hydrological cycle in the region (*3*).

An increase in SASM rainfall and a weakening of the SASM circulation with increasing anthropogenic carbon emissions have been projected by the ensemble mean of the Coupled Model Intercomparison Project Phase 3 (CMIP3) or CMIP5 models (*4*–*6*). Model projections also show changes in the intensity and location of the large-scale systems related to SASM, including the monsoon trough over India, the Mascarene High, the western North Pacific (NP) subtropical high, and the upper tropospheric South Asian high (*7*). However, large uncertainties among individual model projections lead to challenges for adaptation and mitigation planning in this densely populated and ecologically vulnerable region (*2*, *8*). Uncertainties in future emissions scenarios, model's response to a given radiative forcing, and internal climate variations are the three main sources of uncertainty in climate projections (*9*). The uncertainty in future scenarios can be narrowed by a world agreement on climate policy. The model uncertainty is reducible with improved models. While our knowledge on the uncertainties due to the first two sources is improving (*8*, *10*–*12*), the uncertainty in SASM rainfall projections arising from internal climate variability remains unclear, especially for the next few decades (*13*).

Internal variability greatly influences the projected changes in regional rainfall over a period of several decades (*14*, *15*). As a dominant internal mode of the climate system, the Pacific Decadal Oscillation (PDO) or the Interdecadal Pacific Oscillation (IPO) affects the decadal-to-multidecadal rainfall variations over many places around the globe (*16*), including South Asia (*17*–*19*). During the past century, a positive phase of PDO/IPO often leads to decreased SASM rainfall through weakened Walker and monsoon Hadley circulations induced by anomalous sea surface temperatures (SSTs) over the Pacific and vice versa (*18*). The anomalous Pacific SSTs are also substantially related to the frequency and intensity of the droughts over India in observations (*20*). In addition to anthropogenic external forcings (*21*–*23*), the negative-to-positive phase transition of the PDO/IPO explains the total drying trend with similar magnitude to the anthropogenic aerosols over India from 1950 to 1999 (*23*). This suggests that future projections of the SASM rainfall will also depend on the IPO phase evolution. However, how and how much a PDO/IPO phase transition would affect the projected SASM rainfall during the next few decades remain unclear.

Extracting the signals of internal variability requires accurate exclusion of the externally forced changes. Previous climate projections rely heavily on the data of CMIP models. Different CMIP models may include different implementation of the forcings, and the models also differ in dynamical cores and physical package. All of these complicate the interpretation of the differences among the individual model runs (*24*). Instead, a large ensemble by a single model enables us to better quantify the internal variability by using the intermember spread (*14*, *25*, *26*). Recently, a 100-member large ensemble of simulations using the Max Planck Institute Earth System Model (MPI-ESM) version 1.1 has been completed (*27*) and used to understand changes in internal climate variability and their impacts on future climate projections (*28*–*30*). As the largest ensemble currently available using a comprehensive climate model under different forcing scenarios, it allows us to consider the ensemble mean as the externally forced signal, while the differences among the individual members are considered to arise mainly from internal variability (see Materials and Methods). We further use another 50-member large ensemble from the Canadian Earth System Model version 2 (CanESM2) (*31*, *32*) to verify our results from the MPI-ESM.

RESULTS

The externally forced summer (June-July-August or JJA mean) rainfall changes seen in the ensemble mean of the MPI-ESM simulations

[1]LASG, Institute of Atmospheric Physics, Chinese Academy of Sciences, Beijing 100029, China. [2]University of Chinese Academy of Sciences, Beijing 100049, China. [3]CAS Center for Excellence in Tibetan Plateau Earth Sciences, Chinese Academy of Sciences (CAS), Beijing 100101, China. [4]Department of Atmospheric and Environmental Sciences, University at Albany, State University of New York, Albany, NY, USA. [5]Max Planck Institute for Meteorology, Hamburg, Germany.
*Corresponding author. Email: zhoutj@lasg.iap.ac.cn

show an increasing trend of 0.31 mm day^{-1} (30 years)$^{-1}$ ($P < 0.01$) from 2016 to 2045 over the SASM region (5°N to 30°N, 65° to 90°E; Fig. 1A) under the representative concentration pathway 8.5 (RCP8.5) high emissions scenario. However, there is a large uncertainty in this rainfall trend as shown by its large standard deviation (SD) across the ensemble members (Fig. 1B). With the same external forcing, the 100 ensemble members predict diverse SASM rainfall changes, which are illustrated by the different composites of the 10 members with the lowest SASM rainfall trend (hereinafter referred to as Dry10; Fig. 1C) and the 10 members with the highest trends (hereinafter referred to as Wet10; Fig. 1D). The SASM rainfall trend during 2016–2045 ranges from −0.78 to 1.17 mm day^{-1} (30 years)$^{-1}$ with a 5th to 95th percentile range of 1.33 mm day^{-1} (30 years)$^{-1}$, and 75 of the 100 realizations show positive trends (Fig. 1E). The average trend in the Dry10 and Wet10 is −0.35 and 1.02 mm day^{-1} (30 years)$^{-1}$, respectively. Thus, internal variability eclipses the externally forced change in SASM rainfall, leading to very different trends during 2016–2045 among the individual realizations.

To identify the internal climate mode responsible for the spread in the projected SASM rainfall, we calculated the rainfall and SST trend differences between the Dry10 and the Wet10 members (hereinafter referred to as Dry10-Wet10; Fig. 2). The SST trend difference features a warming tropical central-eastern Pacific (TCEP) and a cooling NP (Fig. 2B), which resembles the observed IPO pattern (*16*) and also the IPO-related SST anomalies in the MPI-ESM (fig. S2). The leading empirical orthogonal function 1 (EOF1) mode of the 100 maps of the JJA land rainfall trend over the SASM domain (see Materials and Methods), which explains 34% of the total variance, reveals the dominant spatial pattern of the uncertainty in the projected rainfall trend. This EOF1 pattern is also significantly correlated with the IPO-like SST trend pattern (fig. S3). These results indicate a potential link between different realizations of the IPO phase and the spread in the SASM rainfall projection among the 100 simulations.

The 100 realizations indeed have diverse IPO phase evolutions during the period of 2016 to 2045, as reflected by the different trends in the IPO index (see Materials and Methods; fig. S4). Among the 100 realizations, the projected SASM rainfall trends are negatively correlated ($r = -0.42$, $P < 0.01$) with the IPO index trends (Fig. 2C). This suggests that the SASM rainfall trends are related to the IPO phase transitions. Previous studies have shown that the observed variability of the SASM rainfall was influenced by the IPO-related SST anomalies through large-scale atmospheric circulation changes (*16*–*18*). Accompanying different IPO evolutions in the Dry10 and Wet10 members, warm SST anomalies over the TCEP in the Dry10-Wet10 (Fig. 2B) weaken the Walker circulation over the tropical Pacific Ocean (Fig. 2D). The Dry10-Wet10 differences of the 200-hPa velocity potential and the sea level pressure both show an increase trend over the tropical Indian Ocean, indicating anomalous descending motions there, which further leads to weakened southwest monsoon winds (Fig. 2D). The negative correlation between the SASM rainfall and the IPO index and the associated physical processes shown here for the near-term projections are consistent with previous studies on the historical changes (*17*, *18*). Thus, the IPO is one of the key internal modes influencing the near-term projection of SASM rainfall.

To examine whether the projection uncertainty in SASM rainfall would be reduced with improved prediction of the IPO, we chose one of the 100 ensemble members as the target for projection (see Materials and Methods; fig. S5). In each case, the remaining 99 members are categorized on the basis their IPO index trends. The selected members of groups A to C have increasing errors in the standardized IPO index trends during 2016–2045, and they are within the range of −0.5 to 0.5, −1.0 to 1.0, and −2.0 to 2.0 SD (30 years)$^{-1}$ of the reference member, respectively. Compared with the SASM rainfall trend SD of the full ensemble, the average trend SDs of groups A to C are reduced by about 10, 7, and 4%, respectively. Meanwhile, the 5th to 95th percentile range of the rainfall trends is also reduced from 1.33 to 0.97 (a 27% reduction), 1.10 (a 17% reduction), and 1.13 (a 15% reduction) mm day^{-1} (30 years)$^{-1}$, respectively. While the reduction is only modest, it is non-negligible and increases with improved IPO prediction. It suggests that improved prediction of future IPO can lead to a meaningful reduction in the uncertainty of the projected near-term SASM rainfall.

To further quantify how much the projection uncertainty in SASM rainfall could be explained by the IPO phase evolution from 2016 to 2045, we excluded all of the IPO's influence by removing the SASM rainfall variations that are linearly related to the IPO index in each realization (see Materials and Methods). The histograms and the fitted distribution showing the frequency of occurrence of the area-averaged SASM rainfall trends narrow after removing IPO's influence, with the 5th to 95th percentile range reduced by about 15% from 1.33 to 1.13 mm day^{-1} (30 years)$^{-1}$ (Fig. 3A). The SD of the rainfall trends is also reduced by about 13% from 0.40 to 0.35 ($P = 0.20$). While these reductions are still only modest, they are non-negligible and suggest that we can reduce the projection uncertainty by improving our knowledge about the key modes of internal variability related to the SASM rainfall, such as the IPO.

If the near-future IPO's phase and amplitude could be predicted, we could use an "IPO constraint" to adjust the future SASM rainfall trend in each model run (see Materials and Methods). To illustrate this constraint and show the potential impact of IPO phase changes, here, we used the trend of the standardized IPO during a shift from +1 SD to −1 SD or vice versa from 2016 to 2045 for a significant negative-to-positive (IPO+) or a positive-to-negative (IPO−) IPO phase transition, respectively (fig. S4). An IPO phase change of 2 SDs over a 30-year period is a plausible scenario that occurred in the past (*16*). After removing the IPO's influence in each ensemble member through linear regression as mentioned above, we then added back the fixed IPO's influence corresponding to the −2 or +2 SD (30 years)$^{-1}$ IPO trend so that the adjusted SASM rainfall trends include the decadal variation induced by the same IPO phase transition and external forcing among all the model runs, along with other stochastic internal variability (Fig. 3B). If an IPO+ with an amplitude of +2 SD (30 years)$^{-1}$ was predicted to be superimposed onto the external forcing from 2016 to 2045 under the RCP8.5 emission, then the 100 MPI-ESM members would show an average rate of 0.01 mm day^{-1} (30 years)$^{-1}$, which is 0.30 mm day^{-1} (30 years)$^{-1}$ drier than the externally forced trend. The chance of a positive (COP) SASM rainfall trend (see Materials and Methods) would drop from the original 75 to 54%. In the meantime, the chance of an extreme drying (COED) trend (see Materials and Method) would increase from the original 10 to 32%, while the chance of an extreme wetting (COEW) trend (see Materials and Method) would decrease from the original 10 to 1%. In contrast, if an IPO− with an amplitude of −2 SD (30 years)$^{-1}$ was predicted, then the ensemble mean trend would increase from 0.31 to 0.61 mm day^{-1} (30 years)$^{-1}$, with a COP of 96%, a COED of 1%, and a COEW of 24% (Fig. 3B); this

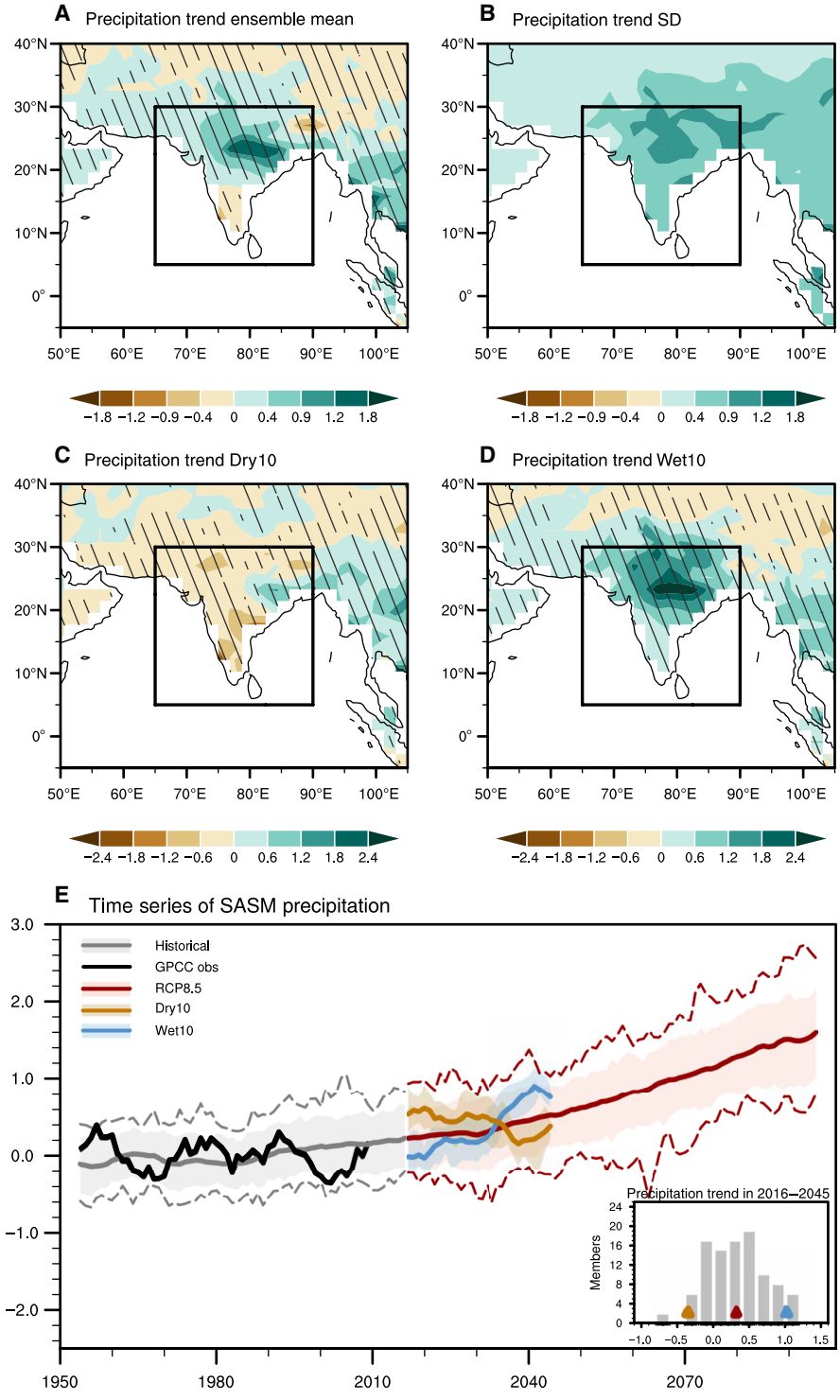

Fig. 1. SASM rainfall changes under the RCP8.5 scenario. June-July-August (JJA) mean rainfall trends under RCP8.5 scenario during 2016–2045 for (**A**) MPI-ESM 100-member ensemble mean, (**B**) intermember SD, (**C**) the mean trend of the 10 members with the driest trends, and (**D**) the mean trend of the 10 members with the wettest trends. Slant hatching denotes trends significant at the 95% confidence level. Units: mm day^{-1} (30 years)$^{-1}$. The box in (A) to (D) highlights the SASM region (5°N to 30°N, 65°E to 90°E). (**E**) Time series of 9-year running mean of SASM rainfall anomalies (relative to the 1950–2005 mean). Historical (gray) and RCP8.5 (red) simulations are shown for the 5th and 95th percentiles (shading), the ensemble mean (thick solid lines), and the maximum and minimum (dashed lines) of the 100 members (units: mm day^{-1}). The black line denotes the observational time series of the 9-year running mean of the SASM rainfall anomalies derived from the Global Precipitation Climatology Centre version v7 dataset. The 10 members with the wettest (blue) and driest (brown) trends during 2016–2045 are also shown together with its 5th and 95th percentile (shading). The inset figure in (E) shows the histogram of the SASM rainfall trends during 2016–2045 for the 100 MPI-ESM members under the RCP8.5 scenario [units: mm day^{-1} (30 years)$^{-1}$]. The red, blue, and brown triangles denote the ensemble mean of the 100 members, the 10 wettest members, and the 10 driest members, respectively.

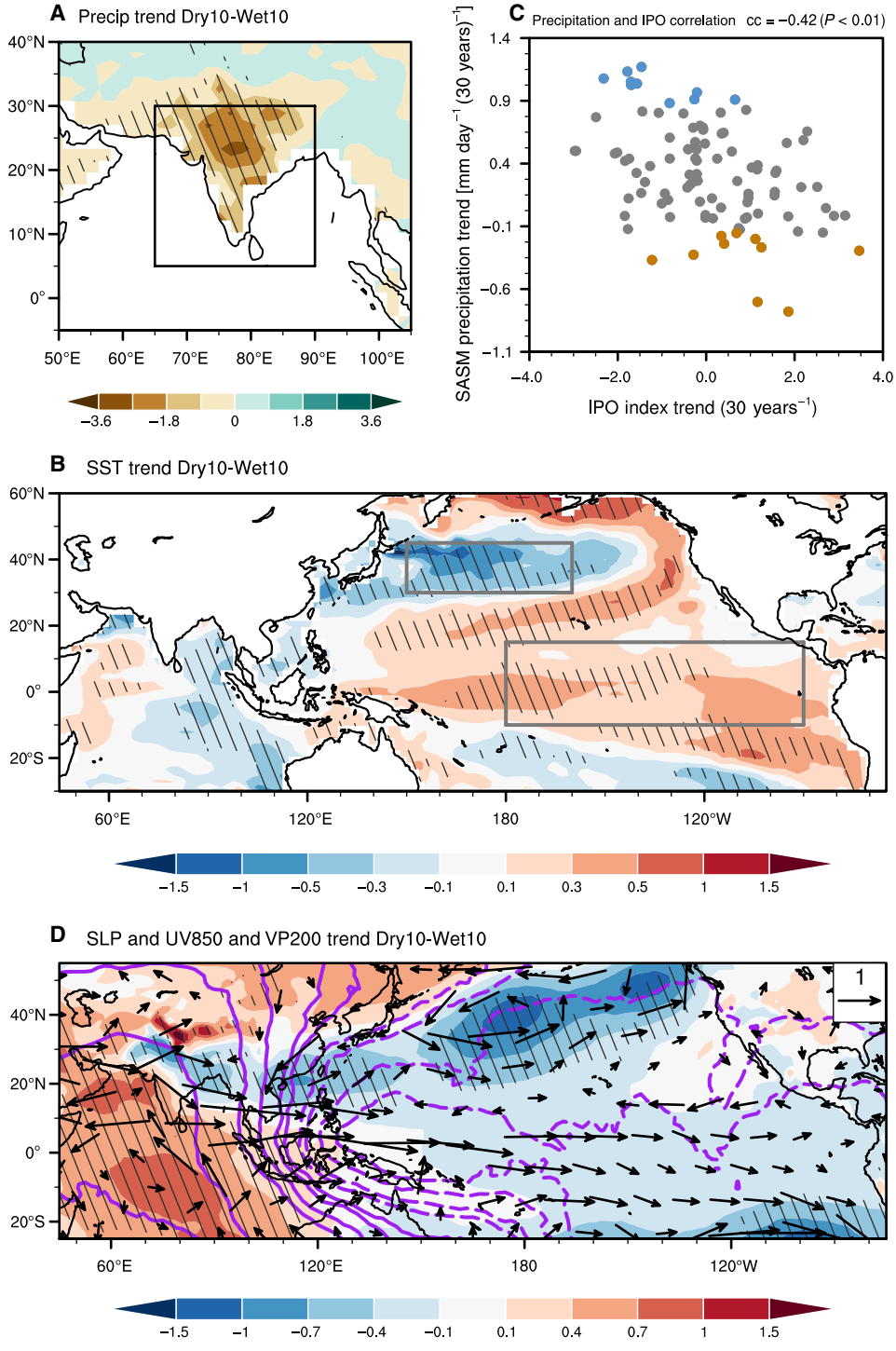

Fig. 2. Trends in SSTs and large-scale circulation associated with SASM rainfall trend spread under the RCP8.5 scenario. (**A**) Mean SASM rainfall trends differences between the 10 members with the driest and the wettest trends during 2016–2045 [units: mm day^{-1} (30 years)$^{-1}$]. (**B**) SST trend differences [units: K (30 years)$^{-1}$] and (**D**) trend differences of the sea level pressure [shading; units: hPa (30 years)$^{-1}$], 200-hPa velocity potential [contours, units: m^2 s^{-1} (30 years)$^{-1}$], and 850-hPa winds [vectors; units: m s^{-1} (30 years)$^{-1}$] during 2016–2045 between the 10 driest and the 10 wettest members of MPI-ESM simulation under the RCP8.5 scenario. Slant hatching denotes regions significant at the 95% confidence level. (**C**) Scatterplot between the standardized IPO index trends [*x* axis; units: (30 years)$^{-1}$] and the SASM rainfall trends [*y* axis; units: mm day^{-1} (30 years)$^{-1}$] among the MPI-ESM 100 members. Blue and brown dots denote the 10 wettest and 10 driest members, respectively.

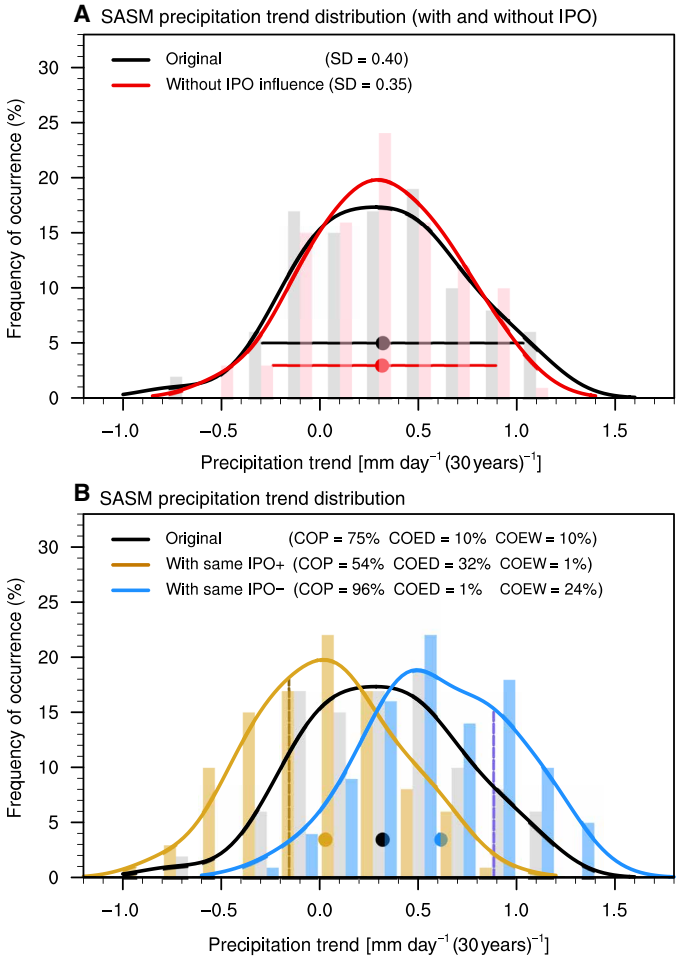

Fig. 3. SASM rainfall trend histograms under the RCP8.5 scenario with and without IPO's influences. (**A**) Histograms (bars) and 100-bins fitted distribution (lines) of the area-averaged rainfall trends over the SASM region (5°N to 30°N, 65°E to 90°E) derived from the 100 MPI-ESM ensemble members. The gray bars and the black fitted curves show the frequency of occurrence of the rainfall trends (with an SD of 0.40). The pink bars and the red fitted curves show the frequency of occurrence of the rainfall trends with the IPO's influence being removed through linear regression against the IPO index in the individual runs (with a SD of 0.35). The black and red dots denote the ensemble mean of the distribution represented by the corresponding color. The black and red horizontal lines denote the 5th to 95th percentile range of 1.33 and 1.13 for the distribution represented by the corresponding color. (**B**) The gray bars and black curves are the same as (A), while the brown and blue bars and curves show the frequency of occurrence of the area-averaged rainfall trends with the same amplitude of a positive [+2 (30 years)$^{-1}$] or a negative [−2 (30 years)$^{-1}$] IPO phase transition, respectively, from 2016 to 2045. The black, brown, and blue dots denote the ensemble mean of the distribution with the corresponding color. The purple (brown) dashed line denotes the threshold of a chance of an extreme wetting (drying) trend.

implies an extremely likely wetting future with more chance of floods but less chance of droughts in the monsoon region. These calculations reveal the large impacts from a plausible IPO phase change on the SASM rainfall and demonstrate that the near-future IPO phase transition has a notable impact on the projected SASM rainfall trend, especially on the occurrence of an extreme wetting or drying trend.

We investigate the robustness of the above results by (i) comparing the results derived from the RCP4.5 scenario with the above findings based on the RCP8.5 scenario using the model (figs. S3, S4, and S6), (ii) comparing the rainfall trend uncertainty based on the next 15 years (2016 to 2030) with the above findings based on the next 30 years (fig. S7), and (iii) comparing the results derived from the MPI-ESM ensemble with another 50-member large ensemble of CanESM2 (Fig. 4 and fig. S8). As expected, the most obvious difference is the external forced rainfall trends in the ensemble mean derived from different emissions scenarios, over different time periods and between different models. Another notable difference is that the estimated IPO's contribution to the projection uncertainty in SASM rainfall is model dependent (Figs. 3 and 4). After removing the IPO-induced rainfall variation via linear regression, the uncertainty in the projected trends measured by the SD among the 50 CanESM2 members is significantly reduced by about 26% from 0.61 to 0.45 ($P < 0.05$; Fig. 4B). The 5th to 95th percentile range of the projected rainfall trends is also reduced by about 30% from 2.31 to 1.61 mm day^{-1} (30 years)$^{-1}$. Despite these quantitative differences, the SASM rainfall trend uncertainty can be, in part, attributed to the internal IPO mode for both emissions scenarios, both the 15- and 30-year time periods (figs. S3, S6, and S7), and are also confirmed by the CanESM2 ensemble (fig. S8). In all the cases, different IPO phase transitions can modulate the magnitude or even reverse the sign of the SASM rainfall trends and affect the occurrence of extreme rainfall changes in the next 15 to 30 years (Figs. 3 and 4 and figs. S6 and S7).

DISCUSSION

By analyzing the large ensemble projections based on the MPI-ESM and CanESM2, we investigated the influence of the IPO-related internal variability on the uncertainty in future SASM rainfall changes. We have shown that internal climate variability can eclipse the externally forced rainfall trend in South Asia during the next 15 to 30 years, leading to large projection uncertainty. We found that the uncertainty in near-future SASM rainfall trends is due, in part, to IPO's future phase evolution by about 13 to 15% in the MPI-ESM ensemble and 26 to 30% in the CanESM2 ensemble.

While the IPO-related uncertainty in near-future SASM projections is non-negligible, the remaining large projection uncertainties indicate the importance of other internal variability. Previous studies suggest that the decadal-scale SASM rainfall variability is also influenced by the Atlantic Multidecadal Oscillation (AMO) (*33*–*35*). Physically, the SST anomalies in the North Atlantic can modulate the meridional tropospheric temperature gradients over South Asia and shift the intertropical convergence zone, which results in anomalous moisture convergence over India. The observed positive correlation between the AMO and the SASM rainfall is reasonably reproduced in the MPI-ESM (fig. S9). After excluding the AMO's influence on the SASM rainfall via linear regression in each realization similar to the analysis done for IPO (see Materials and Methods), the SD and the 5th to 95th percentile range of the rainfall trends during 2016–2045 are reduced by about 3 and 8% in the MPI-ESM ensemble, respectively (fig. S10A). It indicates that the AMO also, in part, helps reduce the projection uncertainty in SASM rainfall, but to a less extent than the IPO. The role of AMO is also confirmed by the CanESM2 ensemble, in which the AMO reduces both the SD and the 5th to 95th percentile range of the SASM rainfall trends by about 10% (fig. S10B).

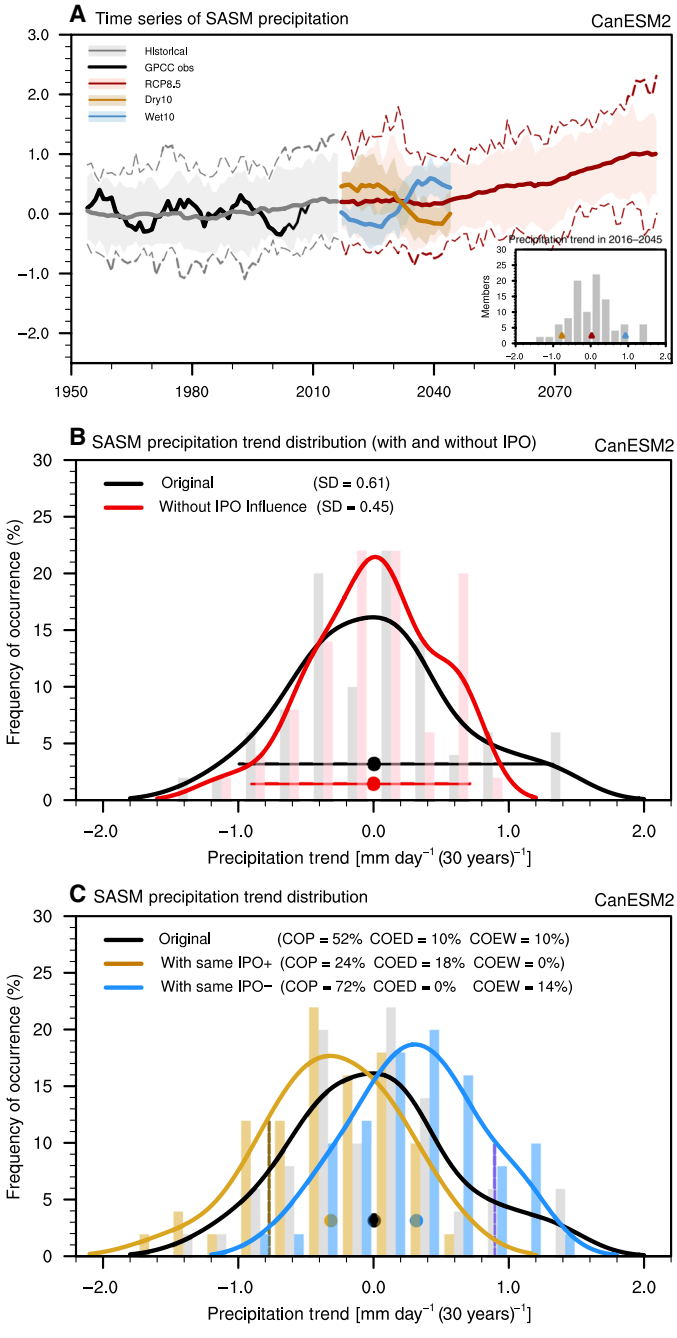

Fig. 4. Uncertainty in the SASM rainfall changes under the RCP8.5 scenario in CanESM2. (**A**) Time series of 9-year running mean of the SASM rainfall anomalies relative to 1950–2005 mean similar to Fig. 1E but derived from the 50 CanESM2 members. (**B** and **C**) Histograms and 100-bins fitted distribution of the area-averaged SASM rainfall trends similar to Fig. 3 but for the 50 CanESM2 members.

For developing effective adaptation and mitigation strategies, decision-makers can hardly be satisfied with an ensemble mean projection without considering internal climate variability. Our study found that the IPO is one of the leading internal modes that partly contribute to the projection uncertainty in near-term SASM rainfall. Accounting for future IPO phase evolution helps reduce the projection uncertainty of near-term SASM rainfall, albeit only by a modest amount; in particular, it improves the projection of an extremely wet or dry condition in South Asia. The Decadal Climate Prediction Project for the CMIP6, which devotes coordinated efforts to improve the predictive skill for IPO (*36*), will likely improve IPO phase predictions for the upcoming decades, which in turn will help improve the near-term SASM projection. Moreover, better understanding and prediction of other decadal-multidecadal modes, such as the AMO, can also improve the near-term SASM projection. Thus, our study calls for further understanding and prediction of the near-term evolutions of the IPO, AMO, and other decadal modes of internal variability to improve the SASM projection.

MATERIALS AND METHODS

Observational data

We used the monthly gridded precipitation data from the Global Precipitation Climatology Centre version 7 (GPCC v7), covering the periods 1901 to 2013 with a horizontal resolution of 0.5° × 0.5° (*37*). Previous study found that the GPCC v6 and new version precipitation datasets are more reliable than other products for estimating global land precipitation changes due to data coverage after the 1990s (*38*).

Observed monthly SST data are taken from the National Oceanic and Atmospheric Administration/National Climatic Data Center Extended Reconstructed SST version 4 (ERSST v4), covering the periods 1901 to 2017 with a horizontal resolution of 2.0° × 2.0° (*39*). Considering about the reliability, we use the SST data after the 1920.

To capture the interdecadal variability in the Pacific, two published indices are used in this study for comparison. One is the PDO index from Mantua and Hare (*40*), and the other is the Tripole index from Henley *et al.* (*41*).

Statistical analysis

A 9-year running mean was applied to rainfall and SST data to isolate the interdecadal signal. The Mann-Kendall nonparametric method (*42*) was applied in this study to test the significance of trends. The Monte Carlo nonparametric method was used to test the significance of regression coefficients onto the filtered time series. To test the significance of the trend differences between the 10 driest and wettest members, the Student's *t* test was used. To test the significance of changes in variance (or SD) of trend spread, the *F* test was used. Eighty of 100 members agreement in signs are used as a threshold to test the member consistency.

Model simulations

MPI-ESM

We used the output from a 100-member Grand Ensemble generated by the MPI-ESM (*27*, *29*). It is an update of the coupled ocean-atmosphere general circulation model submitted to CMIP5 in its low-resolution configuration (MPI-ESM-LR), which has a spectral horizontal resolution of T63/1.9° and 47 vertical layers up to 0.01 hPa in the atmosphere along with 1.5° horizontal resolution and 40 vertical levels in the ocean. Individual ensemble members only differ in their initial conditions, generated by starting the historical simulations in year 1850 from different years, with a random time interval, of the preindustrial control (piControl) simulation. The piControl run has a total length of 2000 years with the forcing constant in time at 1850 values. In this study, the middle 1000-year data from piControl run were used. The historical simulations of the MPI-ESM ensemble

are integrated from 1850 to 2005 driven by observed historical changes in radiative forcing agents including well-mixed greenhouse gases, anthropogenic sulfate aerosols, man-made land-use change, monthly zonal mean ozone concentrations, and major volcanic eruptions following CMIP5 protocol (*43*). The RCP8.5 and RCP4.5 simulations, where the radiative forcing increases and reaches around 8.5 or 4.5 W/m^2 near 2100 relative to 1750, are performed from 2006 to 2099 (*44*).

The reliability of future changes predicted from climate models can be measured by the model's creditability in simulating present-day climate. The MPI-ESM shows reasonable performance in reproducing the climatology of the SASM (fig. S1). The climatological monsoon rainfall centers located near the Western Ghats, over the foothills of the Himalayas, core monsoon regions over the northern-central India and along the Burmese coast are well simulated. Compared to its contemporaries, the parent model, MPI-ESM-LR, is one of the best at simulating the spatial patterns and the onset of SASM rainfall and circulation (*45*).

With respect to the historical variability, the time series of the observational SASM rainfall anomalies is overall within the 5th to 95th percentile envelope of 100 ensemble members (Fig. 1E). The significant decreasing trend of SASM rainfall during the past 30 years (1976–2005) can be reproduced by some of the ensemble members (fig. S1). The performances of the MPI-ESM in reproducing the climatology and historical changes of SASM rainfall aid confidence in our further analysis based on the model.

CanESM2

To help confirm the results derived from the MPI-ESM ensemble, we used the output from another large ensemble of coupled simulations performed with the CanESM2 (*31*, *32*). The CanESM2 is run by the Canadian Center for Climate Modelling and Analysis, which submits five ensemble members to the CMIP5. The CanESM2 large ensemble expanded this initial ensemble by branching each of the original 5 members into 10 members to form a 50-member large ensemble started with slightly different initial conditions at a horizontal resolution of T42/2.8° and 22 vertical layers up to 1 hPa in the atmosphere. The historical simulations of the CanESM2 are integrated from 1950 to 2005 run with both natural (including solar and volcanic) and anthropogenic (including greenhouse gases, aerosol emission, and land use) forcings. The RCP8.5 simulations are performed from 2006 to 2100.

Separating externally forced and internally unforced signal

The 100 members of MPI-ESM ensemble (or the 50 members of CanESM2 ensemble) are driven by the same external forcing. The spread of climate changes obtained from various ensemble members is caused by internal variability arising from random climate variations. The ensemble mean can be taken as the response to external forcing due to the unprecedented ensemble size. Deviations in each ensemble member from the ensemble mean represent internal variability separated from the forced component.

For clarity, the separation of a certain variable (A) of member i in MPI-ESM is calculated as

$$A(i) = A_{\text{forced}} + A_{\text{internal}}(i), i = 1, 2, 3...100 \quad (1)$$

where A_{forced} is the ensemble mean of the 100 members, denoting the response to external forcings. A_{internal} (i) is the residual of the original $A(i)$ minus the forced response. A_{internal} (i) varies among different members and shows the variability associated with internal variability.

Identify the internal mode responsible for the uncertainty

We identify the internal mode responsible for the spread in the projection in two ways. First, we compare the 10 extreme members of the ensemble with the driest (Dry10) and wettest (Wet10) SASM rainfall trends, respectively. The Dry10-Wet10 SST difference indicates the leading internal mode in the ocean related to the rainfall trend uncertainty.

Second, similar to Deser *et al.* (*46*), we compute the leading EOF of the SASM rainfall trends, i.e., land rainfall trends within (5°N to 30°N, 65°E to 90°E) domain, during 2016–2045 across the 100 MPI-ESM members. Here, the member index serves as the time index in a conventional EOF analysis. The 100 values of the corresponding principal component 1 (PC1) are for 100 ensemble members. Then, 100 rainfall and SST trend patterns derived from 100 ensemble members are regressed onto the standardized PC1 at each grid through the member index. This intermember EOF method helps identify the major uncertainty among ensemble members. The regression of SST trend spread on the member index with respect to the PC1 helps find the related internal variability in the ocean.

IPO definition and its contribution to the SASM rainfall trend projection

IPO definition

Previous studies show many different ways to calculate the index representing the IPO/PDO, for example, the EOF method (*40*) and the difference of SST anomalies between the Pacific regions (*23*, *41*), showing an overall similarity in featuring the decadal-to-multidecadal variability of the Pacific SST in the observation after 1920 (*23*, *47*). Thus, for easier calculation and for direct comparison between observation and model simulations and comparison among each ensemble members, we use the latter way to define the IPO index similar to Salzmann and Cherian (*23*) without applying EOF. We define the IPO index as the JJA north-south gradients of unforced SST. In the observation, we remove the linear trend and calculate the SST anomalies averaged within the TCEP (80°E to 90°W, 10°S to 15°N) and the NP (150°E to 160°W, 30°N to 45°N), respectively. The IPO index is defined as the 9-year running mean of the difference in detrended SST between the TCEP and the NP. The 9-year running mean is used to remove interannual variations. We briefly assess this index derived from the ERSST v4 (fig. S2) datasets with two further published PDO/IPO indices. It is highly consistent with the PDO index based on EOF (*40*) and the TPI index based on the SST anomalies (SSTA) difference method (*41*) in both the time evolution and spatial patterns, implying the reasonable tracking of the low-frequency fluctuations in the Pacific Ocean. In this study, we used the term of IPO as we focus on wider Pacific basin phenomenon.

To calculate the IPO index for each MPI-ESM ensemble member in the historical and RCP experiments, we first separate out the internal part of SST, $\text{SST}_{\text{internal}}(i)$, based on Eq. 1. Then, IPO(i, t), the time series of the IPO index for member i, is calculated as the 9-year running mean of the area-averaged difference of JJA $\text{SST}_{\text{internal}}(i)$ between the TCEP and the NP. We assessed the historical IPO-related SST anomalies by regressing the SST(i) with respect to the IPO(i, t) during 1920–2005. With a high intermember consistency, the IPO-related SST anomalies derived from the historical run show

similar spatial characteristics as in the observations and as in the 1000-year piControl run without external forcing (fig. S2), indicating a reasonable performance of the MPI-ESM in simulating the IPO.

The contribution of IPO to the SASM rainfall future projection

We evaluate how much IPO helps to constrain the uncertainty in SASM rainfall projections in two ways. First, we choose one of the 100 ensemble member, member *i*, as the reference simulation with a standardized IPO index trend of $\frac{\partial \mathrm{IPO}(i,t)}{\partial t}$ (30 years)$^{-1}$. $\frac{\partial \mathrm{IPO}(i,t)}{\partial t}$ represents the phase transition of IPO in this period, which ranges from −3.0 to 3.5 (30 years)$^{-1}$ among the 100 members during 2016–2045 (fig. S4). The reference member is the target for projection, while the remaining 99 members are compared with the reference and categorized on the basis of their IPO index trends (fig. S5). The selected member *a* in the group A has a standardized IPO index trend within the range of $\left(\frac{\partial \mathrm{IPO}(i,t)}{\partial t} - 0.5\right) < \frac{\partial \mathrm{IPO}(a,t)}{\partial t} < \left(\frac{\partial \mathrm{IPO}(i,t)}{\partial t} + 0.5\right)$ (30 years)$^{-1}$, representing a "successful" prediction of the future IPO evolution in member *i* [i.e., within the ±0.5 SD (30 years)$^{-1}$ range of the IPO index trend of the target simulation]. The selected member *b* in the group B has a standardized IPO index trend within the range of $\left(\frac{\partial \mathrm{IPO}(i,t)}{\partial t} - 1.0\right) < \frac{\partial \mathrm{IPO}(b,t)}{\partial t} < \left(\frac{\partial \mathrm{IPO}(i,t)}{\partial t} + 1.0\right)$ (30 years)$^{-1}$, representing an "improved" [i.e., ±1 SD (30 years)$^{-1}$] prediction of IPO evolution in member *i*. The selected member *c* in the group C has a standardized IPO index trend within the range of $\left(\frac{\partial \mathrm{IPO}(i,t)}{\partial t} - 2.0\right) < \frac{\partial \mathrm{IPO}(c,t)}{\partial t} < \left(\frac{\partial \mathrm{IPO}(i,t)}{\partial t} + 2.0\right)$ (30 years)$^{-1}$, representing a "poor" [i.e., ±2 SD (30 years)$^{-1}$] prediction of future IPO evolution in member *i*. As shown in fig. S5, the reference member *i* is chosen among the 100 MPI-ESM members in sequence; thus, the members *a*, *b*, and *c* meeting the criteria of the three groups are different for each case. In each case *i*, we calculate the SD and the 5th to 95th percentile ranges of rainfall trends of members in the groups A to C. Then, we compare the mean value of the 100 cases with the rainfall trend SD or 5th to 95th percentile range of the full ensemble. In this way, we quantify how much projection uncertainty in SASM rainfall has been reduced with improved prediction of the future IPO.

Second, if the future IPO evolution could be perfectly predicted, then we cannot quantify its influence by finding the analogs because the 100 ensemble members have different IPO index trends (fig. S4). Thus, to roughly remove all of the IPO's influence, we derive the standardized IPO index for each ensemble member as mentioned above and then remove the SASM rainfall variations that are linearly related to the standardized IPO index through a linear regression. Following previous studies (*48*), the 9-year running mean time series of the SASM rainfall of member *i*, $pr(i, t)$, from 1950 to 2099 is partitioned as

$$pr(i,t) = r(i)_{pr,\mathrm{IPO}} \cdot \mathrm{IPO}(i,t) + pr_{\text{non-IPO}}(i,t), i = 1,2,3...100 \quad (2)$$

where $r(i)_{pr,\mathrm{IPO}} = \frac{\partial pr(i,t)}{\partial \mathrm{IPO}(i,t)}$ is the regression coefficient of the 9-year running mean internal rainfall with respect to the standardized IPO time series within member *i* during 1950–2099. The product of the regression coefficient and the IPO index, $r(i)_{pr,\mathrm{IPO}} \cdot \mathrm{IPO}(i, t)$, represents the IPO-related component of the rainfall anomalies in member *i*. The residual part, $pr_{\text{non - IPO}}(i, t)$, is the IPO-independent rainfall component without the IPO-induced variations for individual run. We then compare the trend spread of $pr(i, t)$ and $pr_{\text{non - IPO}}(i, t)$, i.e., $\frac{\partial pr(i,t)}{\partial t}$ and $\frac{\partial pr_{\text{non-IPO}}(i,t)}{\partial t}$, to quantify the contribution of IPO to the rainfall trend projection (Fig. 3A).

If a certain IPO phase transition is predicted in the future time period τ (i.e., τ = 2016 to 2045 or τ = 2016 to 2030), then we could adjust the rainfall trends in future projections of 100 ensemble members. We first use the above linear regression method between the IPO and the SASM rainfall to remove the IPO's influence in each ensemble member and then add back a fixed IPO's influence so that all the members are considered to be influenced by a same IPO evolution during τ. Compared to the former method of finding analogs, the sample size of 100 remains unchanged in this way, providing sufficient estimation of the uncertainty in projected rainfall trends. On the basis of Eq. 2, we used the "IPO constraint" to adjust the rainfall trend of member *i*, $\frac{\partial \mathrm{pr}_{\mathrm{adj}}(i,t)}{\partial t}$, as

$$\frac{\partial pr_{\mathrm{adj}}(i,t)}{\partial t} = r(i)_{\mathrm{pr,IPO}} \cdot \frac{\partial \mathrm{IPO}(i,t)}{\partial t} + \frac{\partial pr_{\text{non-IPO}}(i,t)}{\partial t}, \quad i = 1,2,3...100 \quad (3)$$

where $\frac{\partial \mathrm{pr}_{\text{non-IPO}}(i,t)}{\partial t}$ is the rainfall trend caused by external forcing and other internal variability except IPO. $\frac{\partial \mathrm{IPO}(i,t)}{\partial t}$ is the trend of the standardized IPO index during time period τ. Here, we use the constant $\frac{\partial \mathrm{IPO}(i,t)}{\partial t} = \pm 2$ (30 years)$^{-1}$ [or ±2 (15 years)$^{-1}$], representing the standardized (SD = 1) IPO index shifting from +1 SD to −1 SD or reversely, as a significant positive/negative IPO phase transition during the analyzing period (fig. S4). Then, we add this fixed $\frac{\partial \mathrm{IPO}(i,t)}{\partial t}$ back to adjust the projected rainfall trends. $r(i)_{pr,\mathrm{IPO}} \cdot \frac{\partial \mathrm{IPO}(i,t)}{\partial t}$ represents the rainfall trend caused by a same IPO phase transition. After the adjustment, the $\frac{\partial \mathrm{pr}_{\mathrm{adj}}(i,t)}{\partial t}$ shows the likely rainfall trend influenced by a certain IPO phase transition (i.e., either positive or negative) at the same magnitude together with the forced changes and other non-IPO internal variability (Fig. 3B).

COP and COEW/COED trend

We used the COP to denote the probability of an increasing SASM rainfall trend in the following 15 to 30 years (Figs. 3 and 4) (*46*). COP is obtained by dividing the number of the MPI-ESM (or CanESM2) members that show positive trends by the total ensemble member (i.e., either 100 for MPI-ESM or 50 for CanESM2). The COP is calculated for both the original rainfall trends $\left(\frac{\partial \mathrm{pr}(i,t)}{\partial t}\right)$ and the adjusted rainfall trends with a certain IPO phase transition $\left(\frac{\partial \mathrm{pr}_{\mathrm{adj}}(i,t)}{\partial t}\right)$.

We used the COEW to denote the probability of an SASM rainfall trend exceeding the 90th percentile of the original rainfall trends ($\frac{\partial pr(i,t)}{\partial t}$; Figs. 3 and 4 and figs. S6 and S7). The COED denotes the probability of an SASM rainfall trend outside the 10th percentile of the original rainfall trends. Thus, COED (COEW) is obtained by dividing the number of the MPI-ESM (or CanESM2) members that show rainfall trends less (greater) than or equal to the 10th (90th) percentile of $\frac{\partial pr(i,t)}{\partial t}$ by the total ensemble member (i.e., either 100 for MPI-ESM or 50 for CanESM2). Thus, the COED and COEW are both 10% for the original rainfall trends. The COED and COEW are also calculated for adjusted rainfall trends with a certain IPO phase transition $\left(\frac{\partial \mathrm{pr}_{\mathrm{adj}}(i,t)}{\partial t}\right)$ in Figs. 3 and 4 and figs. S6 and S7.

Contribution of AMO to the SASM rainfall trend projection

The AMO index is defined as the detrended 9-year running mean area-averaged SST anomalies over the North Atlantic Ocean (80°W to 0°E, 0°N to 65°N). As recommended in previous study (*49*), the detrending here is done by subtracting the global mean (180°W to 180°E, 80°S to 80°N) SST anomaly time series. We assessed the AMO-related SST and SASM rainfall anomalies in the 1000-year

piControl run of the MPI-ESM. The regressed patterns indicate a reasonable performance of the MPI-ESM in simulating the AMO and its positive correlation with the SASM rainfall in the observation (fig. S9).

To evaluate how much the AMO helps constrain the uncertainty in SASM rainfall projections, we derive the standardized AMO index for each ensemble member, i.e., AMO(i, t). We then remove the SASM rainfall variations that are linearly related to the standardized AMO index through a linear regression. Similar as the Eq. 2, the 9-year running mean time series of the SASM rainfall of member i, $pr(i, t)$, from 1950 to 2099 is partitioned as

$$pr(i,t) = r(i)_{pr,\mathrm{AMO}} \cdot \mathrm{AMO}(i,t) + pr_{\text{non-AMO}}(i,t), i = 1,2,3...100 \quad (4)$$

where $r(i)_{pr,\mathrm{AMO}} = \frac{\partial pr(i,t)}{\partial \mathrm{AMO}(i,t)}$ is the regression coefficient of the 9-year running mean internal rainfall with respect to the standardized AMO time series within member i during 1950–2099. The product of the regression coefficient and the AMO index, $r(i)_{pr,\mathrm{AMO}} \cdot \mathrm{AMO}(i, t)$, represents the AMO-related component of the rainfall anomalies in member i. The residual part, $pr_{\text{non - AMO}}(i, t)$, is the AMO-independent rainfall component without the AMO-induced variations for individual run. The trend spread of $pr_{\text{non - AMO}}(i, t)$, i.e., $\frac{\partial pr_{\text{non-AMO}}(i,t)}{\partial t}$, is compared with the above $\frac{\partial pr(i,t)}{\partial t}$ to quantify the contribution of AMO to the rainfall trend projection (fig. S10).

SUPPLEMENTARY MATERIALS

Supplementary material for this article is available at http://advances.sciencemag.org/cgi/content/full/6/11/eaay6546/DC1

Fig. S1. Evaluation of the historical SASM rainfall in MPI-ESM.
Fig. S2. IPO indices and the associated SST anomalies.
Fig. S3. The leading intermember EOF pattern of the SASM rainfall trends and the associated SST trend.
Fig. S4. Trends of IPO indices.
Fig. S5. Analogs among the 100 MPI-ESM ensemble members based on the IPO index trends.
Fig. S6. The influence of IPO evolution on the SASM rainfall trends projection uncertainty under the RCP4.5 scenario.
Fig. S7. The influence of IPO transition on the SASM rainfall trends projection uncertainty during 2016–2030 under the RCP8.5 scenario.
Fig. S8. The trend uncertainty in the SASM rainfall and the associated SST trends under the RCP8.5 scenario in CanESM2.
Fig. S9. AMO-related SASM rainfall and SST anomalies in the observations and MPI-ESM.
Fig. S10. SASM rainfall trend during 2016–2045 under the RCP8.5 scenario without influences of the AMO.

REFERENCES AND NOTES

1. P. Wang, B. Wang, H. Ceng, J. Fasullo, Z. Guo, T. Kiefer, Z. Liu, The global monsoon across time scales: Mechanisms and outstanding issues. *Earth-Sci. Rev.* **174**, 84–121 (2017).
2. A. G. Turner, H. Annamalai, Climate change and the South Asian summer monsoon. *Nat. Clim. Change* **2**, 587–595 (2012).
3. R. Krishnan, T. P. Sabin, R. Vellore, M. Mujumdar, J. Sanjay, B. N. Goswami, F. Hourdin, J. L. Dufresne, P. Terray, Deciphering the desiccation trend of the South Asian monsoon hydroclimate in a warming world. *Clim. Dyn.* **47**, 1007–1027 (2016).
4. R. H. Kripalani, J. H. Oh, A. Kulkarni, S. S. Sabade, H. S. Chaudhari, South Asian summer monsoon precipitation variability: Coupled climate model simulations and projections under IPCC AR4. *Theor. Appl. Climatol.* **90**, 133–159 (2007).
5. R. Krishnan, T. P. Sabin, D. C. Ayantika, A. Kitoh, M. Sugi, H. Murakami, A. G. Turner, J. M. Slingo, K. Rajendran, Will the South Asian monsoon overturning circulation stabilize any further? *Clim. Dyn.* **40**, 187–211 (2012).
6. K. P. Sooraj, P. Terray, M. Mujumdar, Global warming and the weakening of the Asian summer monsoon circulation: Assessments from the CMIP5 models. *Climate Dynam.* **45**, 233–252 (2015).
7. B. Preethi, M. Mujumdar, A. Prabhu, R. H. Kripalani, Variability and teleconnections of South and East Asian summer monsoons in present and future projections of CMIP5 climate models. *Asia-Pac. J. Atmos. Sci.* **53**, 305–325 (2017).
8. X. Chen, T. Zhou, Distinct effects of global mean warming and regional sea surface warming pattern on projected uncertainty in the South Asian summer monsoon. *Geophys. Res. Lett.* **42**, 9433–9439 (2015).
9. E. Hawkins, R. Sutton, The Potential to narrow uncertainty in regional climate predictions. *Bull. Am. Meteorol. Soc.* **90**, 1095–1108 (2009).
10. R. E. Bartlett, M. A. Bollasina, B. B. B. Booth, N. J. Dunstone, F. Marenco, G. Messori, D. J. Bernie, Do differences in future sulfate emission pathways matter for near-term climate? A case study for the Asian monsoon. *Clim. Dynam.* **50**, 1863–1880 (2018).
11. G. Li, S.-P. Xie, C. He, Z. Chen, Western Pacific emergent constraint lowers projected increase in Indian summer monsoon rainfall. *Nat. Clim. Change* **7**, 708–712 (2017).
12. A. Kitoh, The Asian monsoon and its future change in climate models: A review. *J. Meteorol. Soc. Japan Ser II* **95**, 7–33 (2017).
13. E. Hawkins, R. Sutton, The potential to narrow uncertainty in projections of regional rainfall change. *Clim. Dynam.* **37**, 407–418 (2010).
14. C. Deser, R. Knutti, S. Solomon, A. S. Phillips, Communication of the role of natural variability in future North American climate. *Nat. Clim. Change* **2**, 775–779 (2012).
15. A. Dai, C. E. Bloecker, Impacts of internal variability on temperature and precipitation trends in large ensemble simulations by two climate models. *Climate Dynam.* **52**, 289–306 (2019).
16. B. Dong, A. Dai, The influence of the Interdecadal Pacific Oscillation on temperature and precipitation over the globe. *Clim. Dyn.* **45**, 2667–2681 (2015).
17. R. Krishnan, M. Sugi, Pacific decadal oscillation and variability of the Indian summer monsoon rainfall. *Clim. Dyn.* **21**, 233–242 (2003).
18. L. Krishnamurthy, V. Krishnamurthy, Influence of PDO on South Asian summer monsoon and monsoon–ENSO relation. *Clim. Dyn.* **42**, 2397–2410 (2013).
19. M. K. Joshi, A. Rai, Combined interplay of the Atlantic multidecadal oscillation and the interdecadal Pacific oscillation on rainfall and its extremes over Indian subcontinent. *Clim. Dyn.* **44**, 3339–3359 (2015).
20. B. Preethi, R. Ramya, S. K. Patwardhan, M. Mujumdar, R. H. Kripalani, Variability of Indian summer monsoon droughts in CMIP5 climate models. *Clim. Dyn.* **53**, 1937–1962 (2019).
21. M. A. Bollasina, Y. Ming, V. Ramaswamy, Anthropogenic aerosols and the weakening of the South Asian summer monsoon. *Science* **334**, 502–505 (2011).
22. X. Li, M. Ting, C. Li, N. Henderson, Mechanisms of Asian summer monsoon changes in response to anthropogenic forcing in CMIP5 models. *J. Climate* **28**, 4107–4125 (2015).
23. M. Salzmann, R. Cherian, On the enhancement of the Indian summer monsoon drying by Pacific multidecadal variability during the latter half of the twentieth century. *J. Geophys. Res. Atmos.* **120**, 9103–9118 (2015).
24. L. M. Frankcombe, M. H. England, M. E. Mann, B. A. Steinman, Separating internal variability from the externally forced climate response. *J. Climate* **28**, 8184–8202 (2015).
25. C. Hedemann, T. Mauritsen, J. Jungclaus, J. Marotzke, The subtle origins of surface-warming hiatuses. *Nat. Clim. Change* **7**, 336–339 (2017).
26. W. Hua, A. Dai, L. Zhou, M. Qin, H. Chen, An externally forced decadal rainfall seesaw pattern over the sahel and southeast amazon. *Geophys. Res. Lett.* **46**, 923–932 (2019).
27. N. Maher, S. Milinski, L. Suarez-Gutierrez, M. Botzet, M. Dobrynin, L. Kornblueh, J. Kröger, Y. Takano, R. Ghosh, C. Hedemann, C. Li, H. Li, E. Manzini, D. Notz, D. Putrasahan, L. Boysen, M. Claussen, T. Ilyina, D. Olonscheck, T. Raddatz, B. Stevens, J. Marotzke, The Max Planck institute grand ensemble: Enabling the exploration of climate system variability. *J. Adv. Model. Earth Syst.* **11**, 2050–2069 (2019).
28. H. Li, T. Ilyina, Current and future decadal trends in the oceanic carbon uptake are dominated by internal variability. *Geophys. Res. Lett.* **45**, 916–925 (2018).
29. N. Maher, D. Matei, S. Milinski, J. Marotzke, ENSO change in climate projections: Forced response or internal variability? *Geophys. Res. Lett.* **45**, 11390–11398 (2018).
30. J. Marotzke, Quantifying the irreducible uncertainty in near-term climate projections. *Wiley Interdiscip. Rev.* **10**, e563 (2018).
31. M. C. Kirchmeier-Young, F. W. Zwiers, N. P. Gillett, Attribution of extreme events in Arctic Sea Ice Extent. *J. Climate* **30**, 553–571 (2017).
32. M. Sigmond, J. C. Fyfe, Tropical Pacific impacts on cooling North American winters. *Nat. Clim. Change* **6**, 970–974 (2016).
33. R. Zhang, T. L. Delworth, Impact of Atlantic multidecadal oscillations on India/Sahel rainfall and Atlantic hurricanes. *Geophys. Res. Lett.* **33**, 10.1029/2006GL026267, (2006).
34. B. N. Goswami, M. S. Madhusoodanan, C. P. Neema, D. Sengupta, A physical mechanism for North Atlantic SST influence on the Indian summer monsoon. *Geophys. Res. Lett.* **33**, 10.1029/2005GL024803, (2006).
35. L. Krishnamurthy, V. Krishnamurthy, Teleconnections of Indian monsoon rainfall with AMO and Atlantic tripole. *Clim. Dyn.* **46**, 2269–2285 (2015).
36. G. J. Boer, D. M. Smith, C. Cassou, F. Doblas-Reyes, G. Danabasoglu, B. Kirtman, Y. Kushnir, M. Kimoto, G. A. Meehl, R. Msadek, W. A. Mueller, K. E. Taylor, F. Zwiers, M. Rixen, Y. Ruprich-Robert, R. Eade, The Decadal Climate Prediction Project (DCPP) contribution to CMIP6. *Geosci. Model Dev.* **9**, 3751–3777 (2016).

37. U. Schneider, A. Becker, P. Finger, A. Meyer-Christoffer, M. Ziese, B. Rudolf, GPCC's new land surface precipitation climatology based on quality-controlled in situ data and its role in quantifying the global water cycle. *Theor. Appl. Climatol.* **115**, 15–40 (2014).
38. A. Dai, T. Zhao, Uncertainties in historical changes and future projections of drought. Part I: Estimates of historical drought changes. *Clim. Change* **144**, 519–533 (2017).
39. B. Huang, V. F. Banzon, E. Freeman, J. Lawrimore, W. Liu, T. C. Peterson, T. M. Smith, P. W. Thorne, S. D. Woodruff, H. M. Zhang, Extended Reconstructed Sea Surface Temperature Version 4 (ERSST.v4). Part I: Upgrades and intercomparisons. *J. Climate* **28**, 911–930 (2015).
40. N. J. Mantua, S. R. Hare, The Pacific decadal oscillation. *J. Oceanogr.* **58**, 35–44 (2002).
41. B. J. Henley, J. Gergis, D. J. Karoly, S. Power, J. Kennedy, C. K. Folland, A Tripole Index for the Interdecadal Pacific Oscillation. *Clim. Dynam.* **45**, 3077–3090 (2015).
42. A. Mondal, S. Kundu, A. Mukhopadhyay, Rainfall trend analysis by Mann-Kendall test: A case study of north-eastern part of Cuttack district, Orissa. *Int. J. Geol. Earth Sci.* **2**, 70–78 (2012).
43. K. E. Taylor, R. J. Stouffer, G. A. Meehl, An overview of CMIP5 and the experiment design. *Bull. Am. Meteorol. Soc.* **93**, 485–498 (2012).
44. D. P. van Vuuren, J. Edmonds, M. Kainuma, K. Riahi, A. Thomson, K. Hibbard, G. C. Hurtt, T. Kram, V. Krey, J. F. Lamarque, T. Masui, M. Meinshausen, N. Nakicenovic, S. J. Smith, S. K. Rose, The representative concentration pathways: An overview. *Clim. Change* **109**, 5–31 (2011).
45. M. Ashfaq, D. Rastogi, R. Mei, D. Touma, L. R. Leung, Sources of errors in the simulation of south Asian summer monsoon in the CMIP5 GCMs. *Clim. Dyn.* **49**, 193–223 (2017).
46. C. Deser, J. W. Hurrell, A. S. Phillips, The role of the North Atlantic Oscillation in European climate projections. *Clim. Dyn.* **49**, 3141–3157 (2017).
47. W. Hua, A. Dai, M. Qin, Contributions of internal variability and external forcing to the recent pacific decadal variations. *Geophys. Res. Lett.* **45**, 7084–7092 (2018).
48. T. Zhou, R. Yu, H. Li, B. Wang, Ocean forcing to changes in global monsoon precipitation over the recent half-century. *J. Climate* **21**, 3833–3852 (2008).
49. K. E. Trenberth, D. J. Shea, Atlantic hurricanes and natural variability in 2005. *Geophys. Res. Lett.* **33**, (2006).

Acknowledgments: We acknowledge the support from Jiangsu Collaborative Innovation Center for Climate Change. The historical simulations of MPI-ESM ensemble were performed with the Swiss National Computing Centre (CSCS), and the corresponding RCP scenarios simulations were performed with the facilities at the German Climate Computing Centre (DKRZ). We also thank the Canadian Center for Climate Modeling and Analysis for making the CanESM2 ensemble data. We appreciate the comments from B. Stevens of MPI-M that helped us to improve the analysis method. **Funding:** The study is supported by the Strategic Priority Research Program of the Chinese Academy of Sciences (grant no. XDA20060102), International Partnership Program of Chinese Academy of Sciences (grant no. 134111KYSB20160031), and National Natural Science Foundation of China under grant no. 41775091. A.D. was supported by the NSF (grant no. OISE-1743738) and the U.S. National Oceanic and Atmospheric Administration (award nos. NA15OAR4310086 and NA18OAR4310425). C.L. was supported by the Clusters of Excellence CLICCS (EXC2037), University of Hamburg, funded by the German Research Foundation (DFG). X.C. was supported by the National Natural Science Foundation of China under grant no. 41605057. **Author contributions:** T.Z. designed the research, provided comments, and revised the manuscript. X.H. performed the analysis and drafted the manuscript. A.D., H.L., and C.L. helped organize and revise the draft. All of the co-authors contributed to scientific interpretations and helped to improve the manuscript. **Competing interests:** The authors declare that they have no competing interests. **Data and materials availability:** All data needed to evaluate the conclusions in the paper are present in the paper and/or the Supplementary Materials. The observational precipitation and SST datasets are available on the Climate Data Guide website (https://climatedataguide.ucar.edu). The published PDO index of Mantua and Hare (*40*) is available from the University of Washington, USA (www.jisao.washington.edu/pdo). The published TPI index of Henley *et al.* (*41*) can be accessed at www.esrl.noaa.gov/psd/data/timeseries/IPOTPI. The MPI-ESM grand ensemble data are available for noncommercial use via https://esgf-data.dkrz.de/projects/mpi-ge/. Detailed information of the data and references can be found at www.mpimet.mpg.de/en/grand-ensemble/. The data in this study are analyzed with NCAR Command Language (NCL; www.ncl.ucar.edu/). All relevant codes used in this work are available upon request from T.Z. Additional data related to this paper may be requested from the authors.

Submitted 7 July 2019
Accepted 17 December 2019
Published 13 March 2020
10.1126/sciadv.aay6546

Citation: X. Huang, T. Zhou, A. Dai, H. Li, C. Li, X. Chen, J. Lu, J.-S. Von storch, B. Wu, South Asian summer monsoon projections constrained by the interdecadal Pacific oscillation. *Sci. Adv.* **6**, eaay6546 (2020).

South Asian summer monsoon projections constrained by the interdecadal Pacific oscillation

Xin Huang, Tianjun Zhou, Aiguo Dai, Hongmei Li, Chao Li, Xiaolong Chen, Jingwen Lu, Jin-Song Von storch and Bo Wu

Sci Adv **6** (11), eaay6546.
DOI: 10.1126/sciadv.aay6546